First principle investigation of halogen-doped monolayer g-C$_3$N$_4$ photocatalyst

Bicheng Zhu [a], Jinfeng Zhang [a], Chuanjia Jiang [a], Bei Cheng [a], Jiaguo Yu [a,b,*]

[a] State Key Laboratory of Advanced Technology for Materials Synthesis and Processing, Wuhan University of Technology, Wuhan 430070, PR China
[b] Department of Physics, Faculty of Science, King Abdulaziz University, Jeddah 21589, Saudi Arabia

ARTICLE INFO

ABSTRACT

Element doping is an efficient strategy for tuning the electronic structure and improving the photocatalytic activity of graphitic carbon nitride (g-C$_3$N$_4$). Employing the density functional theory computation performed by CASTEP module, we investigated the band structures, electronic and optical properties of monolayer g-C$_3$N$_4$ doped with halogens (F, Cl, Br or I). First, the halogen atoms occupying the interstitial space enclosed by three tri-s-triazine units in the monolayer g-C$_3$N$_4$ unit cell was demonstrated to be the most stable configuration in terms of adsorption energy. On the basis of these interstitial-doped monolayer g-C$_3$N$_4$ systems, it is found that the introduction of halogen atoms leads to various density of states (DOS) and redistribution of the lowest unoccupied molecular orbital (LUMO) and the highest occupied molecular orbital (HOMO). The F atom tends to occupy the valance band and HOMO due to its extremely high electronegativity. By contrast, the Cl, Br and I atoms are involved in the conduction band and LUMO. In sum, the calculation results show that the halogen-doped monolayer g-C$_3$N$_4$ systems have narrowed band gap, increased light absorption and reduced work function, which are conducive to high photocatalytic activity. The conclusions presented in this work indicate the availability of halogen-doped monolayer g-C$_3$N$_4$ with considerable photocatalytic performance.

1. Introduction

Graphitic carbon nitride (g-C$_3$N$_4$) is an attractive semiconductor which exhibits enormous application prospect in photocatalysis and adsorption [1,2]. On the one hand, its narrow band gap and appropriate band potential endow it with photocatalytic performance for hydrogen generation [3–5], CO$_2$ reduction [6–8], and pollutants degradation [9,10]. On the other hand, it was investigated as adsorbent to adsorb metal ions [11–13], flavonoids [14], dyes [15], and perfluorinated compounds [16,17]. Unfortunately, suffering from small specific surface area and serious recombination of photogenerated electron–hole pairs, pristine g-C$_3$N$_4$ synthesized by facile calcination method has very limited photocatalytic activity and adsorption capacity. Unremitting efforts have been made to overcome these two deficiencies in order to obtain considerable and practical photocatalytic and adsorption performance.

First, the surface area of g-C$_3$N$_4$ can be increased by various strategies such as ultrasound exfoliation [18,19], chemical exfoliation [20], chemical oxidation [21], thermal oxidation "etching" [22], SiO$_2$ template synthesis [23,24], protonation of precursors [25–28], and so on. Through these efforts, g-C$_3$N$_4$ architectures with various morphologies have emerged, including nanotube [29], hollow sphere [30], nanofiber [31], nanowire [32], nanoribbon [33], and nanosheet [34]. As examples, Yang et al. synthesized ultrathin g-C$_3$N$_4$ nanosheet with thickness of ca. 2 nm and surface area as high as 384 m^2 g^{-1} [35]. In particular, Zhao et al. prepared single layer g-C$_3$N$_4$ with thickness of about 0.5 nm [36], and Xu et al. fabricated monolayer g-C$_3$N$_4$ with thickness of 0.4 nm [20]. In sum, two-dimension ultrathin g-C$_3$N$_4$ layer structure with fewer layers or even monolayer g-C$_3$N$_4$ has become a mainstream for the design of high-efficiency g-C$_3$N$_4$ photocatalysts and adsorbents.

Secondly, many methods have been developed to inhibit the recombination of photogenerated electron–hole pairs, among which constructing composites and doping with other elements are two representative approaches [37–41]. Previous experimental studies demonstrated that nonmetal element doping, such as doping with P, B, C, O, and S was an effective way to enhance the photocatalytic performance of g-C$_3$N$_4$ [42–47]. The immediate cause is that the introduction of these nonmetal elements greatly increased the light absorption and reduced the recombination of photogenerated electron–hole pairs in pristine g-C$_3$N$_4$.

* Corresponding author at: State Key Laboratory of Advanced Technology for Materials Synthesis and Processing, Wuhan University of Technology, Wuhan 430070, PR China.
E-mail addresses: jiaguoyu@yahoo.com, yujiaguo93@163.com (J. Yu).

Meanwhile, intensive theoretical investigations based on first-principle calculations were carried out to elucidate the intrinsic reason for the photocatalytic enhancement effect of element doping. For instance, Ma et al. found that doping g-C_3N_4 with P atom could increase the dispersion of the contour distribution of the lowest unoccupied molecular orbital (LUMO) and the highest occupied molecular orbital (HOMO), thus promoting the charge carrier mobility and facilitating the separation of photogenerated electron–hole pairs [48]. Lin et al. discovered that S-doped g-C_3N_4 followed a different O_2-production reaction mechanism as compared to pure g-C_3N_4, and the introduction of S decreased the overpotential of the reaction [49]. Dong et al. concluded that C atom in C self-doped g-C_3N_4 led to the formation of delocalized big π bond, which was conducive to electron transfer [50].

It can be predicted that introducing impurity element in ultrathin or monolayer g-C_3N_4 could simultaneously overcome the aforementioned two deficiencies. Few experimental studies have been reported, while theoretical investigations have made initial attempts. For example, Ruan et al. revealed the effect of Li doping on the physical properties of monolayer g-C_3N_4 by the first-principle calculations [51]. Cui et al. investigated the geometric and electronic properties of O-doped monolayer g-C_3N_4 model [52].

Halogen doped g-C_3N_4 photocatalysts were successfully synthesized by calcinating the mixture of ammonium halide and the precursors of g-C_3N_4. The introduction of these halogen atoms highly improved the photocatalytic activity of g-C_3N_4 towards hydrogen production, dye degradation, CO_2 reduction, NO removal and benzene oxidation [53–56]. Further, Lu et al. investigated the effects of a series of nonmetal dopants on the chemical performances and physical properties of g-C_3N_4 by first-principle approach using VASP code [57]. In their research, the nonmetal dopants were directly placed at the dicoordinated nitrogen atoms to construct the doping models. Indeed, the dicoordinated nitrogen atoms are generally considered as the active sites of photocatalytic reactions [58]. In reality, however, the doping sites are usually evaluated by formation energies [59,60], and the most stable doping site is not always the dicoordinated nitrogen atoms [48]. Herein, we first determined the most likely doping sites of halogen atoms in monolayer g-C_3N_4 in terms of formation energies, and then systematically studied the effect of halogen atoms doping on the electronic and optical properties of monolayer g-C_3N_4 using CASTEP module.

2. Computational details

Density functional theory (DFT) calculations were performed with CASTEP module on the basis of the plane-wave-pseudo-potential approach. The Perdew–Burke–Ernzerhof (PBE) functional of the generalized gradient approximation (GGA) was used as the exchange–correlation function. The ultrasoft pseudo-potential was employed to describe the interaction between valence electrons and the ionic core. A kinetic energy cutoff of 450 eV and Monkhorst–Pack special k-point meshes of $3 \times 3 \times 1$ were proposed to carry out geometry optimization and electronic structure calculation. During the geometry optimization, all atoms were allowed to relax without any constraints until the convergence thresholds of maximum displacement, maximum force and energy were smaller than 0.001 Å, 0.03 eV/Å and 1.0×10^{-5} eV/atom, respectively.

3. Results and discussion

3.1. Optimized structure of monolayer g-C_3N_4

Before the introduction of halogen atoms, the geometric and electronic structures of pure monolayer g-C_3N_4 were investigated. The monolayer g-C_3N_4 model was built by cleaving the unit cell of
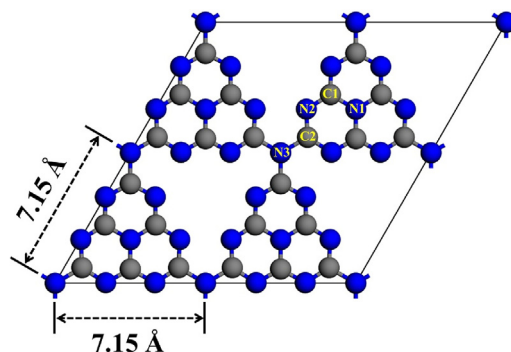
Fig. 1. Optimized structure of monolayer g-C_3N_4. The blue and gray balls represent N and C atoms, respectively. (For interpretation of the references to colour in this figure legend, the reader is referred to the web version of this article.)
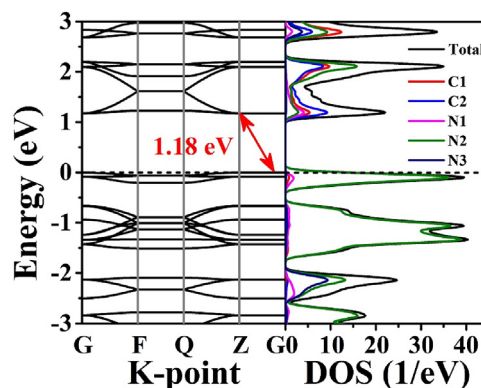
Fig. 2. Calculated band structure and corresponding DOS of monolayer g-C_3N_4. G, F, Q and Z are high symmetry points in the reciprocal space. The short dash line set at zero is treated as the Fermi level.

bulk g-C_3N_4 along the (001) plane [51]. The constructed model is $2 \times 2 \times 1$ supercell containing 24 C atoms and 32 N atoms. A large vacuum space of 15 Å in the z direction was applied to eliminate the effect of interactions between layers. After geometry optimization, the in-plane lattice constant of the g-C_3N_4 model is 7.15 Å (Fig. 1), which is in good accordance with previous computational data and experimental result revealed by X-ray diffraction pattern [52,61,62]. Based on the symmetry of the tri-s-triazine structure of g-C_3N_4, there are three nonequivalent nitrogen atoms and two nonequivalent carbon atoms, which are labelled as N1, N2, N3, C1 and C2, respectively (Fig. 1) [63]. The bond lengths of N1—C1, C1—N2, N2—C2 and C2—N3 are 1.39 Å, 1.33 Å, 1.34 Å and 1.47 Å, respectively, quite consistent with the results in other DFT calculation [64].

3.2. Electronic properties of monolayer g-C_3N_4

The calculated band structure and corresponding density of states (DOS) of monolayer g-C_3N_4 are presented in Fig. 2. It is found that the monolayer g-C_3N_4 is an indirect band gap semiconductor with a band gap energy (E_g) of 1.18 eV. The valance band top (VBT) lies between the Z and G points, and the conduction band bottom (CBB) is located at the Z point. The DOS shows that the valance band (VB) is mainly dominated by the N2 atoms, and the conduction band (CB) is composed of the C1 and C2 atoms and small amounts of N1 and N2 atoms. To intuitively recognize the composition of the band edge, the LUMO and HOMO of monolayer g-C_3N_4 are illustrated in Fig. 3. The HOMO covers all N2 atoms, and the LUMO is mainly distributed on C1 and C2 atoms and moderately occupies N1 and N2 atoms, which conforms to the DOS. It is noted that the
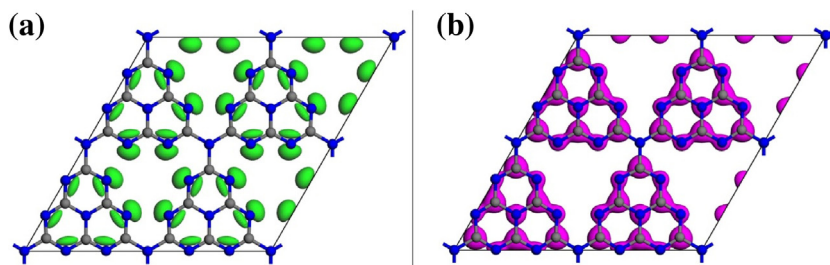
Fig. 3. Calculated HOMO (a) and LUMO (b) of monolayer g-C$_3$N$_4$. The isovalue is set as 0.05 electron/Å^3.

tricoordinated bridge N (N3) atoms do not participate in the VB or CB edge. In other words, no electrons would be excited from N3 atoms under light irradiation, and the photogenerated electrons can neither migrate to N3 atoms nor transfer from one heptazine (C$_6$N$_7$) unit to the adjacent unit through N3 atoms [52]. In this case, the photogenerated electron–hole pairs are localized in each heptazine unit and their separation is inefficient, resulting in poor photocatalytic activity.

3.3. Formation energy of F/Cl-doped monolayer g-C$_3$N$_4$

The F/Cl-doped monolayer g-C$_3$N$_4$ models were built by introducing one F or Cl atom into the 2 × 2 × 1 supercell of monolayer g-C$_3$N$_4$. Normally, the possible doping modes include the impurity atom substituting three kinds of N (N1, N2, N3) or two kinds of C (C1, C2) atoms, and occupying the center of the interstitial space enclosed by three heptazine units. Given that the atomic radii of F and Cl atoms (0.41 Å and 0.78 Å) are close to those of N and C atoms (0.54 Å and 0.65 Å) [65], all these doping modes are feasible

for the introduction of F and Cl atoms. The obtained doping concentrations are 1.79 at.% for the substitution modes and 1.75 at.% for the interstitial mode, which closely approach the experimentally determined boron doping concentration of 1.73 at.% [66].

Fig. 4 shows the optimized structures of F-doped monolayer g-C$_3$N$_4$ with various doping scenarios. It is found that the introduction of F atom leads to displacement of the neighboring atoms and

Table 1
Formation energies (eV) of F/Cl-doped monolayer g-C$_3$N$_4$ systems with various doping sites and chemical conditions.

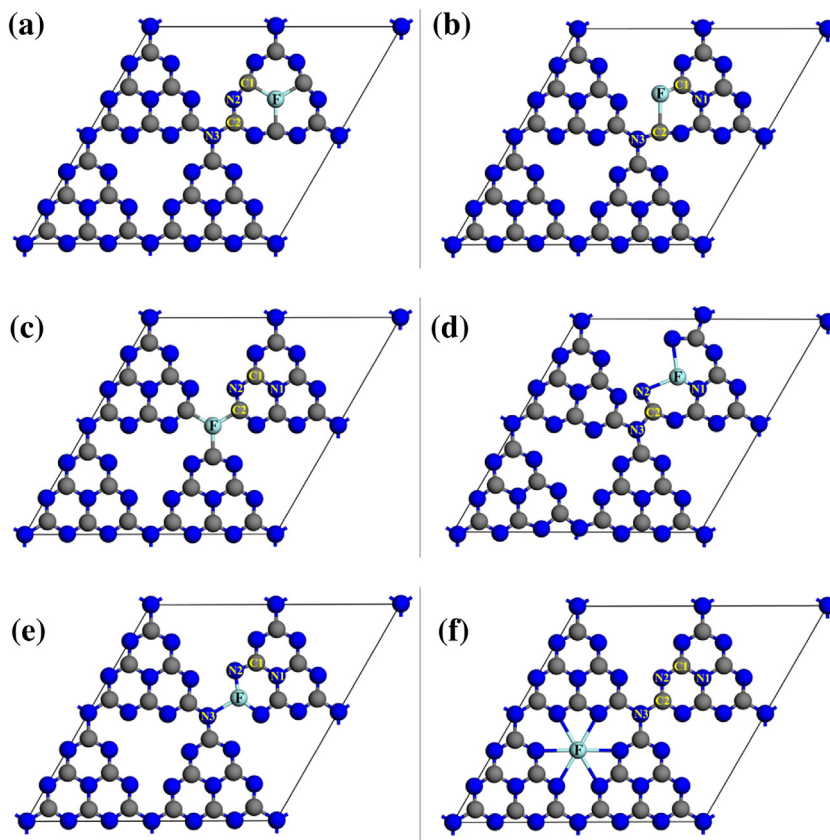| Doping site	F		Cl	
	C-rich	N-rich	C-rich	N-rich
N1	1.53	1.36	7.27	7.10
N2	1.58	1.41	3.77	3.60
N3	4.91	4.74	8.36	8.19
C1	1.87	2.09	5.71	5.93
C2	4.89	5.11	6.79	7.02
Interstitial	1.15	1.15	3.52	3.52

Fig. 4. Optimized structures of F-doped monolayer g-C$_3$N$_4$ with F atom substituting (a) N1, (b) N2, (c) N3, (d) C1 and (e) C2 atoms, and F atom occupying (f) the center of the interstitial space.
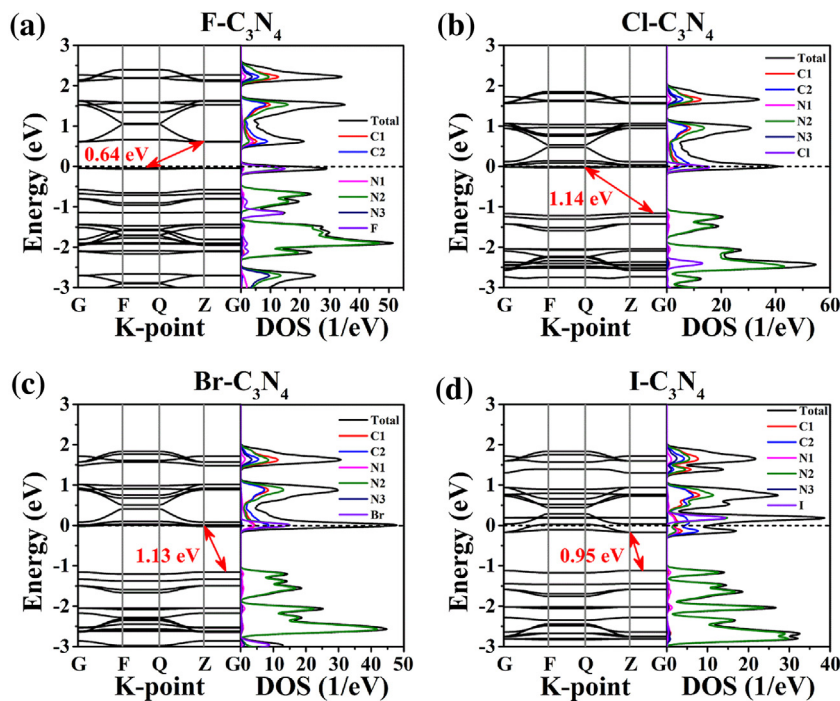
Fig. 5. Calculated band structure and corresponding DOS of halogen interstitial-doped monolayer g-C_3N_4.

deformation of the heptazine unit. The same atomic displacements are also observed in the Cl-doped monolayer g-C_3N_4 models with similar moving directions and distances, hence the optimized structures for Cl-doping are not shown here. To determine the most likely doping site, the defect formation energies (E_{Form}) are calculated using the following equations:

$$E_{Form} = E(X\text{-}C_3N_4) - E(C_3N_4) - \mu(X) + \mu(N) \tag{1}$$

$$E_{Form} = E(X\text{-}C_3N_4) - E(C_3N_4) - \mu(X) + \mu(C) \tag{2}$$

$$E_{Form} = E(X\text{-}C_3N_4) - E(C_3N_4) - \mu(X) \tag{3}$$

where X represents the halogen atom, $E(X\text{-}C_3N_4)$ is the total energy of X-doped g-C_3N_4 system, $E(C_3N_4)$ is the total energy of monolayer g-C_3N_4, $\mu(X)$, $\mu(N)$ and $\mu(C)$ are the chemical potentials of single X, N and C atoms, respectively. Specifically, equations 1–3 are used to calculate the E_{Form} of the doping systems for substituting N, substituting C and occupying interstitial space, respectively. In addition, $\mu(X)$ is obtained by $\mu(X) = \mu(X_2)/2$. The calculations of $\mu(N)$ and $\mu(C)$ depend on specific chemical conditions. Under C-rich condition, $\mu(C)$ is defined as $\mu(C) = \mu(graphene)/18$, and $\mu(N)$ is obtained from the following relationship:

$$4\mu(N) + 3\mu(C) = \mu(C_3N_4) \tag{4}$$

under N-rich condition, $\mu(N)$ is defined as $\mu(N) = \mu(N_2)/2$, and $\mu(C)$ is obtained from Eq. (4). According to these definitions, a smaller formation energy generally corresponds to a thermodynamically more stable system and a more likely doping scenario.

Table 1 lists the calculated formation energies of the various F/Cl-doping systems. All the formation energies are positive, suggesting that all the doping processes are endothermic and thermodynamically non-spontaneous [67]. For both F-doping and Cl-doping circumstances, the formation energies of N-site doping systems under N-rich condition are lower than those under C-rich condition, and similarly, the formation energies of C-site doping systems under C-rich condition are smaller than those under N-rich condition. This finding suggests that one element can be replaced more easily when it is rich in the chemical condition. Meanwhile, all the formation energies of Cl-doped monolayer g-C_3N_4 systems

are higher than those of the F-doped monolayer g-C_3N_4 systems with the same doping site and chemical condition. The more difficult introduction of Cl atoms is due to the larger atomic radius of Cl than that of F [68]. The smallest formation energies (1.15 eV and 3.52 eV) are obtained in the interstitial doping modes for both F-doping and Cl-doping systems. Therefore, the most likely doping mode is interstitial doping with F or Cl atom occupying the center of the interstitial space.

3.4. Formation energy of Br/I-doped monolayer g-C_3N_4

Unlike the moderate atomic radii of F and Cl atoms, the atomic radii of Br and I atoms (1.03 Å and 1.39 Å) are much larger (ca. 1.6–2.6 times) than those of N and C atoms (0.54 Å and 0.65 Å) [65]. It would be very unstable to replace N or C atoms by Br or I atoms. Hence, the five substitutional doping modes are not considered for the construction of Br/I-doped monolayer g-C_3N_4 systems. Here, the Br and I atoms are directly introduced into the interstitial space to obtain Br/I interstitial-doped monolayer g-C_3N_4 systems with the same doping concentration. Using Eq. (3), the formation energies are calculated to be 3.67 eV and 3.36 eV for Br- and I-doping, respectively. At this point, the formation energies of halogen-doped monolayer g-C_3N_4 systems are fully examined. The following sections would focus on the band structures, work functions, electronic and optical properties of halogen interstitial-doped monolayer g-C_3N_4 systems.

3.5. Electronic properties of halogen interstitial-doped monolayer g-C_3N_4

The calculated band structures and DOS of halogen interstitial-doped monolayer g-C_3N_4 are shown in Fig. 5. Based on these results, the band gaps, locations of VBT and CBB, and constitutions of VB and CB are summarized in Table 2. It is found that the band gap of g-C_3N_4 is narrowed after the introduction of halogen atoms into the interstitial space. More specifically, the band gap decreases with increasing atomic numbers of the impurity halogen atoms except F. The CB of F-doped g-C_3N_4 still comprises C1, C2, N1 and N2 atoms,
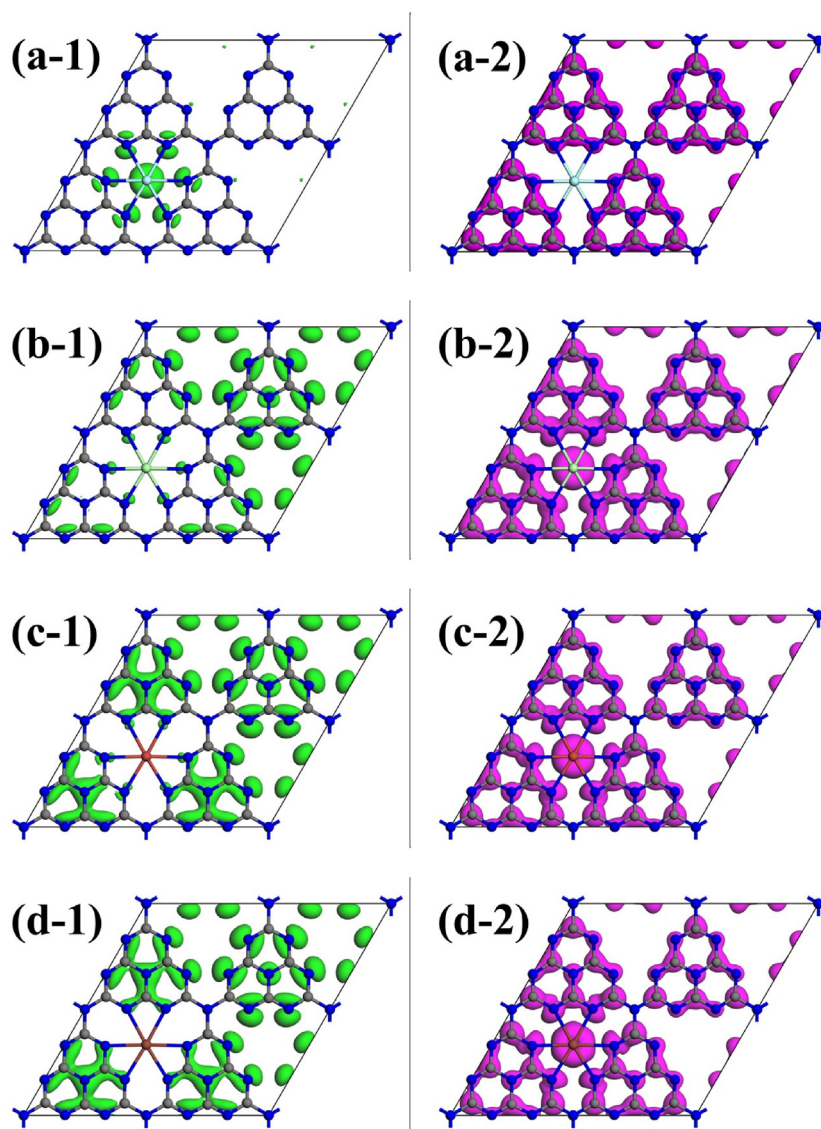
Fig. 6. Calculated HOMO of (a-1) F-, (b-1) Cl-, (c-1) Br- and (d-1) I- doped g-C_3N_4. Calculated LUMO of (a-2) F-, (b-2) Cl-, (c-2) Br- and (d-2) I- doped g-C_3N_4. The isovalue is set as 0.05 electron/$Å^3$.

Table 2
Calculated band gaps, locations of VBT and CBB, and constitutions of VB and CB.

System	E_g (eV)	Location		Nature of band gap	Constitution	
		VBT	CBB		VB	CB
C_3N_4	1.18	Between Z and G	Z	Indirect	N2	C1, C2, N1, N2
F-C_3N_4	0.64	Between F and Q	Z	Indirect	N2, F	C1, C2, N1, N2
Cl-C_3N_4	1.14	Between Z and G	Q	Indirect	N2	Cl, C1, C2, N1, N2
Br-C_3N_4	1.13	Between Z and G	Z	Indirect	N2	Br, C1, C2, N1, N2
I-C_3N_4	0.95	Between Z and G	Z	Indirect	N2	I, C1, C2, N1, N2

while the VB is dominated by N2 and F atoms. As for the Cl, Br and I doped g-C_3N_4, the impurity atoms participate in the constitution of CB, and other ingredients of CB and VB remain unchanged. The peculiarity of F-doped g-C_3N_4 may be ascribed to the strong electronegativity of F. In addition, all the doped g-C_3N_4 systems have indirect band structures with CBB located at the Z or Q point and VBT located between two high symmetry points.

The calculated HOMO and LUMO of halogen interstitial-doped monolayer g-C_3N_4 are presented in Fig. 6. In comparison with the HOMO of pure g-C_3N_4 in Fig. 3a, certain redistribution of HOMO is observed in the halogen interstitial-doped g-C_3N_4. In detail, the HOMO of F-doped g-C_3N_4 contains both F and the surrounding N2 atoms. As for the Cl, Br and I doped g-C_3N_4, the HOMO on the N2 atoms around the halogen atoms becomes weaker and that on N1 atoms appears. The distribution of the LUMO of halogen doped g-C_3N_4 shows no obvious change as compared with that of pure g-C_3N_4, except that the Cl, Br and I atoms occur extensively in the LUMO. These results are consistent with the DOS analysis that the
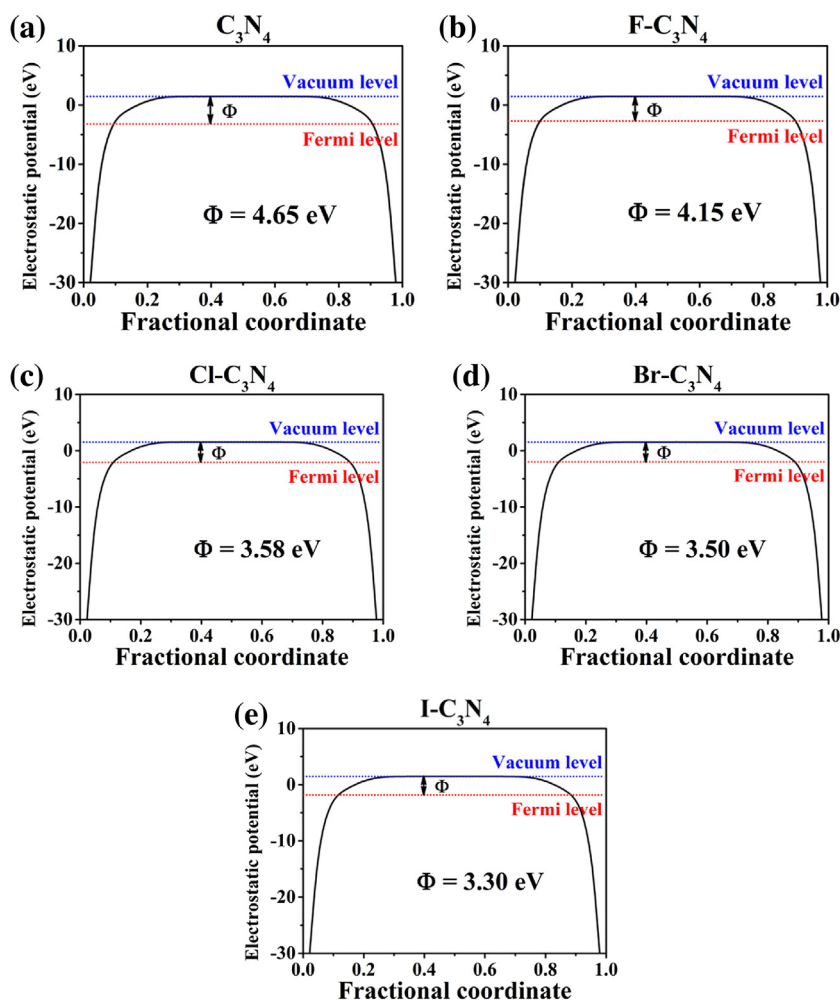
Fig. 7. Work functions of pure (a) and F- (b), Cl- (c), Br- (d), I- (e) doped g-C$_3$N$_4$. The blue and red dash lines are the vacuum level and Fermi level, respectively. (For interpretation of the references to colour in this figure legend, the reader is referred to the web version of this article.)

F atom is contained in the VB and other halogen atoms (Cl, Br and I) are involved in the CB. Besides, the Mulliken charges of the halogen atoms in these doping systems are calculated to be −0.44 e, −0.05 e, 0.39 e and 1.22 e for F, Cl, Br and I, respectively, which corresponds to the descending electronegativity from F to I.

3.6. Work function

Work function is defined as the minimum energy required for an electron to escape from the Fermi level into vacuum. According to this definition, the work function is calculated using the equation $\Phi = E_{Vac} − E_F$, where E_{Vac} and E_F are the potentials of the vacuum level and Fermi level, respectively [69,70]. Fig. 7 shows the obtained work functions of pure and halogen doped g-C$_3$N$_4$. The work function of pure g-C$_3$N$_4$ is 4.65 eV, which is exactly the same as the value reported by Ruan et al. [51]. After the introduction of halogen atoms, the work function of g-C$_3$N$_4$ decreases with increasing atomic numbers of the impurity halogen atoms. This finding may be intrinsically related to the electronegativity. As the atomic number of the halogen atoms increases and the electronegativity decreases, more electrons transfer from the halogen atoms to g-C$_3$N$_4$, thus leading to the gradually uplifted Fermi levels and reduced work functions. In sum, the doping of halogen atoms facilitates the escaping of the electron from the g-C$_3$N$_4$ surface.

3.7. Light absorption

The optical absorption properties of pure and halogen-doped monolayer g-C$_3$N$_4$ are evaluated by absorption coefficient $\alpha(\omega)$ defined as:

$$\alpha(\varpi) = \sqrt{2}\varpi[\sqrt{\varepsilon_1(\varpi)^2 + \varepsilon_2(\varpi)^2} - \varepsilon_1(\varpi)]^{1/2} \qquad (5)$$

where ω is the light frequency, $\varepsilon_1(\omega)$ and $\varepsilon_2(\omega)$ are the real part and imaginary part in the dielectric function, respectively [71]. Fig. 8 shows the calculated optical absorption coefficients as a function of wavelength. It can be seen that the halogen doped g-C$_3$N$_4$ systems exhibit enhanced light absorption in the whole spectral region of 200–1000 nm.

3.8. Various doping concentrations

In the experimental synthesis of element doped g-C$_3$N$_4$, various doping concentrations can be achieved by varying experiment conditions. To investigate the availability of various doping concentrations, we take F element as an example and design four monolayer g-C$_3$N$_4$ models with 1–4 interstitially doped F atoms. The doping concentrations for these models are 1.75, 3.45, 5.08 and 6.67 at.%. The doping formation energies are determined according to the equation $E_{Form(n)} = E(nF\text{-}C_3N_4) − E(C_3N_4) − n\mu(F)$, where n is the number of introduced F atoms (n = 1, 2, 3 or 4),
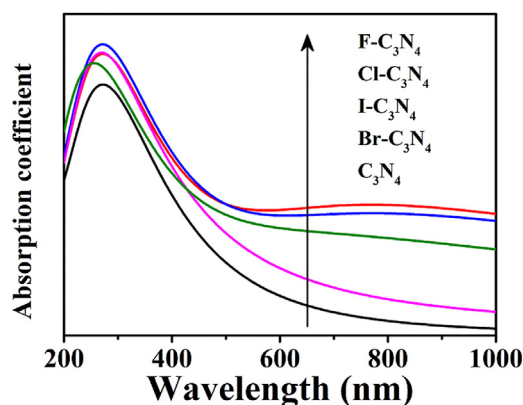
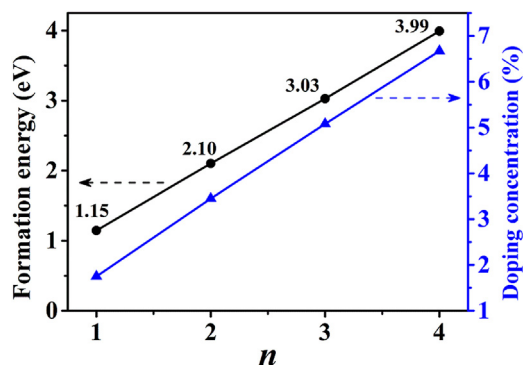**Fig. 8.** Calculated optical absorption coefficients of pure and halogen-doped monolayer g-C$_3$N$_4$.

Fig. 9. Variation of F doping concentrations and corresponding formation energies of F-doped g-C$_3$N$_4$ versus the number of introduced F atoms (n). The numbers above the data points are the formation energies.

and $E(n\text{F-C}_3\text{N}_4)$ is the total energy of the g-C$_3$N$_4$ systems interstitially doped with n F atoms. Fig. 9 shows the variation of doping concentrations and corresponding formation energies versus n. It is found that the formation energy increases linearly with n. Moreover, the difference of the formation energies between adjoining data points is 0.93–0.96 eV, lower than $E_{\text{Form}(1)}$ (1.15 eV). This indicates that it is easier to introduce a F atom into F-doped g-C$_3$N$_4$ than into pure g-C$_3$N$_4$. Therefore, in the experimental synthesis of F-doped g-C$_3$N$_4$, once the experiment condition satisfies the introduction of the first F atom into the g-C$_3$N$_4$ lattice, the subsequent introduction of more F atoms can take place continuously until the experiment condition is changed or F atoms are exhausted. As a consequence, the synthesis of F-doped g-C$_3$N$_4$ with high doping concentration is feasible and controllable. For example, Wang et al. prepared F-doped g-C$_3$N$_4$ sheets with various doping concentrations by changing the dosage of NH$_4$F in the precursors [53].

4. Conclusions

In summary, the band structures, electronic properties, optical properties and work functions of pure and halogen (F, Cl, Br, I) doped monolayer g-C$_3$N$_4$ were examined and investigated by first-principle calculations. Based on the formation energies, the halogen atoms preferentially dope into the interstitial space enclosed by three tri-s-triazine units. The introduction of halogen atoms decreases the band gap from 1.18 eV to 0.64–1.14 eV. The nature of the band gap of both pure and halogen-doped monolayer g-C$_3$N$_4$ is characteristic of indirect semiconductor. The F atom contributes to the valance band while other halogen atoms participate in the conduction band. Correspondingly, the F atom is involved in

the HOMO while other halogen atoms are located in the LUMO. The halogen doped g-C$_3$N$_4$ systems exhibit enhanced optical absorption in a wide wavelength range of 200–1000 nm and reduced work functions. This calculation work provides meaningful instructions for the design of nonmetal doped g-C$_3$N$_4$ photocatalyst.

References

[1] J. Wen, J. Xie, X. Chen, X. Li, A review on g-C$_3$N$_4$-based photocatalysts, Appl. Surf. Sci. 391 (2017) 72–123.
[2] Y. Sun, W. Ha, J. Chen, H. Qi, Y. Shi, Advances and applications of graphitic carbon nitride as sorbent in analytical chemistry for sample pretreatment: a review, TrAC Trends Anal. Chem. 84 (2016) 12–21.
[3] S. Cao, J. Yu, g-C$_3$N$_4$-based photocatalysts for hydrogen generation, J. Phys. Chem. Lett. 5 (2014) 2101–2107.
[4] S. Cao, J. Jiang, B. Zhu, J. Yu, Shape-dependent photocatalytic hydrogen evolution activity over a Pt nanoparticle coupled g-C$_3$N$_4$ photocatalyst, Phys. Chem. Chem. Phys. 18 (2016) 19457–19463.
[5] J. Jiang, J. Yu, S. Cao, Au/PtO nanoparticle-modified g-C$_3$N$_4$ for plasmon-enhanced photocatalytic hydrogen evolution under visible light, J. Colloid Interface Sci. 461 (2016) 56–63.
[6] S. Ye, R. Wang, M. Wu, Y. Yuan, A review on g-C$_3$N$_4$ for photocatalytic water splitting and CO$_2$ reduction, Appl. Surf. Sci. 358 (2015) 15–27.
[7] P. Xia, B. Zhu, J. Yu, S. Cao, M. Jaroniec, Ultra-thin nanosheet assemblies of graphitic carbon nitride for enhanced photocatalytic CO$_2$ reduction, J. Mater. Chem. A (2016), http://dx.doi.org/10.1039/C6TA08310B.
[8] Q. Huang, J. Yu, S. Cao, C. Cui, B. Cheng, Efficient photocatalytic reduction of CO$_2$ by amine-functionalized g-C$_3$N$_4$, Appl. Surf. Sci. 358 (2015) 350–355.
[9] S. Lam, J. Sin, A.R. Mohamed, A review on photocatalytic application of g-C$_3$N$_4$/semiconductor (CNS) nanocomposites towards the erasure of dyeing wastewater, Mater. Sci. Semicond. Process. 47 (2016) 62–84.
[10] B. Zhu, P. Xia, Y. Li, W. Ho, J. Yu, Fabrication and photocatalytic activity enhanced mechanism of direct Z-scheme g-C$_3$N$_4$/Ag$_2$WO$_4$ photocatalyst, Appl. Surf. Sci. 391 (2017) 175–183.
[11] M. Anbia, M. Haqshenas, Adsorption studies of Pb(II) and Cu(II) ions on mesoporous carbon nitride functionalized with melamine-based dendrimer amine, Int. J. Environ. Sci. Technol. 12 (2015) 2649–2664.
[12] H. Chen, T. Yan, F. Jiang, Adsorption of Cr(VI) from aqueous solution on mesoporous carbon nitride, J. Taiwan Inst. Chem. Eng. 45 (2014) 1842–1849.
[13] C. Shen, C. Chen, T. Wen, Z. Zhao, X. Wang, A. Xu, Superior adsorption capacity of g-C$_3$N$_4$ for heavy metal ions from aqueous solutions, J. Colloid Interface Sci. 456 (2015) 7–14.
[14] X. Ding, J. Zhu, Y. Zhang, Q. Xia, W. Bi, X. Yang, J. Yang, Separation and concentration of natural products by fast forced adsorption using well-dispersed velvet-like graphitic carbon nitride with response surface methodology optimisation, Talanta 154 (2016) 119–126.
[15] B. Zhu, P. Xia, W. Ho, J. Yu, Isoelectric point and adsorption activity of porous g-C$_3$N$_4$, Appl. Surf. Sci. 344 (2015) 188–195.
[16] T. Yan, H. Chen, F. Jiang, X. Wang, Adsorption of perfluorooctane sulfonate and perfluorooctanoic acid on magnetic mesoporous carbon nitride, J. Chem. Eng. Data 59 (2014) 508–515.
[17] T. Yan, H. Chen, X. Wang, F. Jiang, Adsorption of perfluorooctane sulfonate (PFOS) on mesoporous carbon nitride, RSC Adv. 3 (2013) 22480–22489.
[18] X. Zhang, X. Xie, H. Wang, J. Zhang, B. Pan, Y. Xie, Enhanced photoresponsive ultrathin graphitic-phase C$_3$N$_4$ nanosheets for bioimaging, J. Am. Chem. Soc. 135 (2013) 18–21.
[19] J. Tian, Q. Liu, A.M. Asiri, A.O. Al-Youbi, X. Sun, Ultrathin graphitic carbon nitride nanosheet: a highly efficient fluorosensor for rapid ultrasensitive detection of Cu^{2+}, Anal. Chem. 85 (2013) 5595–5599.
[20] J. Xu, L. Zhang, R. Shi, Y. Zhu, Chemical exfoliation of graphitic carbon nitride for efficient heterogeneous photocatalysis, J. Mater. Chem. A 1 (2013) 14766–14772.
[21] H.J. Li, B.W. Sun, L. Sui, D.J. Qian, M. Chen, Preparation of water-dispersible porous g-C$_3$N$_4$ with improved photocatalytic activity by chemical oxidation, Phys. Chem. Chem. Phys. 17 (2015) 3309–3315.
[22] P. Niu, L. Zhang, G. Liu, H. Cheng, Graphene-like carbon nitride nanosheets for improved photocatalytic activities, Adv. Funct. Mater. 22 (2012) 4763–4770.
[23] J. Sun, J. Zhang, M. Zhang, M. Antonietti, X. Fu, X. Wang, Bioinspired hollow semiconductor nanospheres as photosynthetic nanoparticles, Nat. Commun. (2012) 1139.
[24] J. Liang, Y. Zheng, J. Chen, J. Liu, D. Hulicova-Jurcakova, M. Jaroniec, S.Z. Qiao, Facile oxygen reduction on a three-dimensionally ordered macroporous

graphitic C_3N_4/carbon composite electrocatalyst, Angew. Chem. Int. Ed. 51 (2012) 3892–3896.

[25] M. Wu, J. Yan, X. Zhang, M. Zhao, Synthesis of g-C_3N_4 with heating acetic acid treated melamine and its photocatalytic activity for hydrogen evolution, Appl. Surf. Sci. 354 (2015) 196–200.

[26] H. Yan, Y. Chen, S. Xu, Synthesis of graphitic carbon nitride by directly heating sulfuric acid treated melamine for enhanced photocatalytic H_2 production from water under visible light, Int. J. Hydro. Energy 37 (2012) 125–133.

[27] X. Zhang, J. Hu, H. Jiang, Facile modification of a graphitic carbon nitride catalyst to improve its photoreactivity under visible light irradiation, Chem. Eng. J. 256 (2014) 230–237.

[28] Y. Zhong, Z. Wang, J. Feng, S. Yan, H. Zhang, Z. Li, Z. Zou, Improvement in photocatalytic H_2 evolution over g-C_3N_4 prepared from protonated melamine, Appl. Surf. Sci. 295 (2014) 253–259.

[29] J. Gao, Y. Zhou, Z. Li, S. Yan, N. Wang, Z. Zou, High-yield synthesis of millimetre-long, semiconducting carbon nitride nanotubes with intense photoluminescence emission and reproducible photoconductivity, Nanoscale 4 (2012) 3687–3692.

[30] Y. Jun, E.Z. Lee, X. Wang, W.H. Hong, G.D. Stucky, A. Thomas, From melamine-cyanuric acid supramolecular aggregates to carbon nitride hollow spheres, Adv. Funct. Mater. 23 (2013) 3661–3667.

[31] M. Tahir, C. Cao, N. Mahmood, F.K. Butt, A. Mahmood, F. Idrees, S. Hussain, M. Tanveer, Z. Ali, I. Aslam, Multifunctional g-C_3N_4 nanofibers: a template-free fabrication and enhanced optical, electrochemical, and photocatalyst properties, ACS Appl. Mater. Interfaces 6 (2014) 1258–1265.

[32] K. Zhang, L. Wang, X. Sheng, M. Ma, M.S. Jung, W. Kim, H. Lee, J.H. Park, Tunable bandgap energy and promotion of H_2O_2 oxidation for overall water splitting from carbon nitride nanowire bundles, Adv. Energy Mater. 6 (2016) 1502352.

[33] Y. Zhao, F. Zhao, X. Wang, C. Xu, Z. Zhang, G. Shi, L. Qu, Graphitic carbon nitride nanoribbons: graphene-assisted formation and synergic function for highly efficient hydrogen evolution, Angew. Chem. Int. Ed. 53 (2014) 13934–13939.

[34] K. Schwinghammer, M.B. Mesch, V. Duppel, C. Ziegler, J. Senker, B.V. Lotsch, Crystalline carbon nitride nanosheets for improved visible-light hydrogen evolution, J. Am. Chem. Soc. 136 (2014) 1730–1733.

[35] S. Yang, Y. Gong, J. Zhang, L. Zhan, L. Ma, Z. Fang, R. Vajtai, X. Wang, P.M. Ajayan, Exfoliated graphitic carbon nitride nanosheets as efficient catalysts for hydrogen evolution under visible light, Adv. Mater. 25 (2013) 2452–2456.

[36] H. Zhao, H. Yu, X. Quan, S. Chen, Y. Zhang, H. Zhao, H. Wang, Fabrication of atomic single layer graphitic-C_3N_4 and its high performance of photocatalytic disinfection under visible light irradiation, Appl. Catal. B: Environ. 152–153 (2014) 46–50.

[37] S. Cao, J. Low, J. Yu, M. Jaroniec, Polymeric photocatalysts based on graphitic carbon nitride, Adv. Mater. 27 (2015) 2150–2176.

[38] W. Yu, D. Xu, T. Peng, Enhanced photocatalytic activity of g-C_3N_4 for selective CO_2 reduction to CH_3OH via facile coupling of ZnO: a direct Z-scheme mechanism, J. Mater. Chem. A 3 (2015) 19936–19947.

[39] J. Yu, S. Wang, J. Low, W. Xiao, Enhanced photocatalytic performance of direct Z-scheme g-C_3N_4-TiO_2 photocatalysts for the decomposition of formaldehyde in air, Phys. Chem. Chem. Phys. 15 (2013) 16883–16890.

[40] Y. Liu, R. Wang, Z. Yang, H. Du, Y. Jiang, C. Shen, K. Liang, A. Xu, Enhanced visible-light photocatalytic activity of Z-scheme graphitic carbon nitride/oxygen vacancy-rich zinc oxide hybrid photocatalysts, Chin. J. Catal. 36 (2015) 2135–2144.

[41] J. Yu, K. Wang, W. Xiao, B. Cheng, Photocatalytic reduction of CO_2 into hydrocarbon solar fuels over g-C_3N_4-Pt nanocomposite photocatalysts, Phys. Chem. Chem. Phys. 16 (2014) 11492–11501.

[42] B. Chai, J. Yan, C. Wang, Z. Ren, Y. Zhu, Enhanced visible light photocatalytic degradation of Rhodamine B over phosphorus doped graphitic carbon nitride, Appl. Surf. Sci. 391 (2017) 376–383.

[43] N. Sagara, S. Kamimura, T. Tsubota, T. Ohno, Photoelectrochemical CO_2 reduction by a p-type boron-doped g-C_3N_4 electrode under visible light, Appl. Catal. B: Environ. 192 (2016) 193–198.

[44] Y. Li, S. Wu, L. Huang, J. Wang, H. Xu, H. Li, Synthesis of carbon-doped g-C_3N_4 composites with enhanced visible-light photocatalytic activity, Mater. Lett. 137 (2014) 281–284.

[45] S. Guo, Y. Zhu, Y. Yan, Y. Min, J. Fan, Q. Xu, Holey structured graphitic carbon nitride thin sheets with edge oxygen doping via photo-Fenton reaction with enhanced photocatalytic activity, Appl. Catal. B: Environ. 185 (2016) 315–321.

[46] K. Wang, Q. Li, B. Liu, B. Cheng, W. Ho, J. Yu, Sulfur-doped g-C_3N_4 with enhanced photocatalytic CO_2-reduction performance, Appl. Catal. B: Environ. 176–177 (2015) 44–52.

[47] Q. Fan, J. Liu, Y. Yu, S. Zuo, B. Li, A simple fabrication for sulfur doped graphitic carbon nitride porous rods with excellent photocatalytic activity degrading RhB dye, Appl. Surf. Sci. 391 (2017) 360–368.

[48] X. Ma, Y. Lv, J. Xu, Y. Liu, R. Zhang, Y. Zhu, A strategy of enhancing the photoactivity of g-C_3N_4 via doping of nonmetal elements: a first-principles study, J. Phys. Chem. C 116 (2012) 23485–23493.

[49] S. Lin, X. Ye, X. Gao, J. Huang, Mechanistic insight into the water photooxidation on pure and sulfur-doped g-C_3N_4 photocatalysts from DFT calculations with dispersion corrections, J. Mol. Catal. A: Chem. 406 (2015) 137–144.

[50] G. Dong, K. Zhao, L. Zhang, Carbon self-doping induced high electronic conductivity and photoreactivity of g-C_3N_4, Chem. Commun. 48 (2012) 6178–6180.

[51] L. Ruan, G. Xu, L. Gu, C. Li, Y. Zhu, Y. Lu, The physical properties of Li-doped g-C_3N_4 monolayer sheet investigated by the first-principles, Mater. Res. Bull. 66 (2015) 156–162.

[52] J. Cui, S. Liang, X. Wang, J. Zhang, First principle modeling of oxygen-doped monolayer graphitic carbon nitride, Mater. Chem. Phys. 161 (2015) 194–200.

[53] Y. Wang, Y. Di, M. Antonietti, H. Li, X. Chen, X. Wang, Excellent visible-light photocatalysis of fluorinated polymeric carbon nitride solids, Chem. Mater. 22 (2010) 5119–5121.

[54] C. Liu, Y. Zhang, F. Dong, A.H. Reshak, L. Ye, N. Pinna, C. Zeng, T. Zhang, H. Huang, Chlorine intercalation in graphitic carbon nitride for efficient photocatalysis, Appl. Catal. B: Environ. 203 (2017) 465–474.

[55] Z. Lan, G. Zhang, X. Wang, A facile synthesis of Br-modified g-C_3N_4 semiconductors for photoredox water splitting, Appl. Catal. B: Environ. 192 (2016) 116–125.

[56] H. Li, Y. Liu, Y. Cui, W. Zhang, C. Fu, X. Wang, Facile synthesis and enhanced visible-light photoactivity of $DyVO_4$/g-C_3N_4I composite semiconductors, Appl. Catal. B: Environ. 183 (2016) 426–432.

[57] S. Lu, C. Li, H.H. Li, Y.F. Zhao, Y.Y. Gong, L.Y. Niu, X.J. Liu, T. Wang, The effects of nonmetal dopants on the electronic, optical and chemical performances of monolayer g–C_3N_4 by first-principles study, Appl. Surf. Sci. 392 (2017) 966–974.

[58] H. Wu, L. Liu, S. Zhao, The role of the defect on the adsorption and dissociation of water on graphitic carbon nitride, Appl. Surf. Sci. 358 (2015) 363–369.

[59] J. Yu, P. Zhou, Q. Li, New insight into the enhanced visible-light photocatalytic activities of B-, C- and B/C-doped anatase TiO_2 by first-principles, Phys. Chem. Chem. Phys. 15 (2013) 12040–12047.

[60] P. Zhou, J. Yu, Y. Wang, The new understanding on photocatalytic mechanism of visible-light response NS codoped anatase TiO_2 by first-principles, Appl. Catal. B: Environ. 142–143 (2013) 45–53.

[61] S.M. Aspera, H. Kasai, H. Kawai, Density functional theory-based analysis on O_2 molecular interaction with the tri-s-triazine-based graphitic carbon nitride, Surf. Sci. 606 (2012) 892–901.

[62] M.J. Bojdys, J.O. Müller, M. Antonietti, A. Thomas, Ionothermal synthesis of crystalline condensed, graphitic carbon nitride, Chem. Eur. J. 14 (2008) 8177–8182.

[63] J. Liu, Effect of phosphorus doping on electronic structure and photocatalytic performance of g-C_3N_4: Insights from hybrid density functional calculation, J. Alloys Compd. 672 (2016) 271–276.

[64] S.M. Aspera, M. David, H. Kasai, First-principles study of the adsorption of water on tri-s-triazine-based graphitic carbon nitride, Jpn. J. Appl. Phys. 49 (2010) 115703.

[65] D.C. Ghosh, R. Biswas, Theoretical calculation of absolute radii of atoms and ions. Part 1. The atomic radii, Int. J. Mol. Sci. 3 (2002) 87–113.

[66] C. Lu, R. Chen, X. Wu, M. Fan, Y. Liu, Z. Le, S. Jiang, S. Song, Boron doped g-C_3N_4 with enhanced photocatalytic UO_2^{2+} reduction performance, Appl. Surf. Sci. 360 (2016) 1016–1022.

[67] L. Ruan, Y. Zhu, L. Qiu, Y. Lu, Mechanical properties of doped g-C_3N_4 –A first-principle study, Vacuum 106 (2014) 79–85.

[68] W. Yu, J. Zhang, T. Peng, New insight into the enhanced photocatalytic activity of N-, C- and S-doped ZnO photocatalysts, Appl. Catal. B: Environ. 181 (2016) 220–227.

[69] J. Liu, B. Cheng, J. Yu, A new understanding of the photocatalytic mechanism of the direct Z-scheme g-C_3N_4/TiO_2 heterostructure, Phys. Chem. Chem. Phys. (2016) 31175–31183.

[70] J. Liu, Origin of high photocatalytic efficiency in monolayer g-C_3N_4/CdS heterostructure: a hybrid DFT study, J. Phys. Chem. C 119 (2015) 28417–28423.

[71] J. Wang, Z. Guan, J. Huang, Q. Li, J. Yang, Enhanced photocatalytic mechanism for the hybrid g-C_3N_4/MoS_2 nanocomposite, J. Mater. Chem. A 2 (2014) 7960–7966.